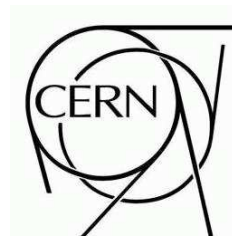


ATLAS NOTE



Measurements from Supersymmetric Events

The ATLAS Collaboration¹⁾

This note is part of CERN-OPEN-2008-020. This version of the note should not be cited: all citations should be to CERN-OPEN-2008-020.

Abstract

We review the techniques used to reconstruct the decay of supersymmetric particles and measure their properties with ATLAS at the LHC, concentrating on strategies to be applied to a data set of integrated luminosity of 1 fb^{-1} that can be expected after the first year of operation of the LHC. These techniques are illustrated using several benchmark points chosen in the mSUGRA parameter space, but they are applicable to a broader range of supersymmetric (and other similar) models. The most appropriate methods will be selected and fine-tuned once (and if) signatures consistent with Supersymmetry are established. Supersymmetric cascade decays typically have large transverse missing energy due to the presence of undetected neutralinos, and have characteristic edges and thresholds in the dilepton, dijet and lepton-jet invariant mass distributions. The reconstruction of such edges is the focus of the first part of the paper. The second part of the paper concentrates on the reconstruction of more specific decay channels, involving light stops, staus and Higgs bosons. The final section indicates how sparticle masses and other supersymmetric parameters could be constrained using such measurements.

¹⁾This note prepared by P. Bechtle, M. Consonni, M. Cooke, D. Costanzo, U. De Sanctis, B. Gjelsten, S. Haug, A. Kastanas, J. Krstic, T. Lari, A. Lipniacka, M. Milosavljevic, S. Montesano, T. Nattermann, N. Ozturk, T.B. Sjursen, A. Tonoyan, C. Topfel, C. Troncon, M. Uhlenbrock, N. Venturi, M. Weber, P. Wienemann, C. Zender.



1 Introduction

Supersymmetry (SUSY) can be discovered by the ATLAS experiment at the LHC during the initial running period if some coloured sparticles have masses of the order hundreds of GeV and hence production cross-sections of the order of a few pb. A strategy to establish SUSY discovery is outlined in another paper in this collection [1], while here we concentrate on parameter measurements that can be performed with the early data. The same particle identification conventions and selection criteria as in [2] are used in this paper.

Once a signature consistent with Supersymmetry has been established, the experimental emphasis will move on to measuring the sparticle mass spectrum and constraining the parameters of the model. In the case of R-parity-conserving models, the decay chain of sparticles cannot be completely reconstructed, as sparticles eventually decay into LSPs that can not be detected. For this reason edge positions, rather than mass peaks, are measured in the invariant mass distribution of sparticle decay products. In R-parity-violating models sparticles can have long lifetimes and can be detected by studying their decay in-flight within the detector. These types of signatures are discussed in [3].

A complete coverage of all allowed SUSY models is impossible, so we limit this study to a subset of the models where SUSY breaking is mediated by gravity (mSUGRA), and to the points in parameter space described in [2], however the measurement techniques and fit methods developed can be adapted for many models. During initial data-taking, the error on such measurements will be limited by statistics, making measurements possible only for models with moderate ($\lesssim 1$ TeV) values of the SUSY mass scale where enough events can be isolated. In this paper we study the cases of a total integrated luminosity of 0.5 fb^{-1} for the ‘‘Low Mass’’ point (SU4) and of 1 fb^{-1} for the ‘‘Bulk’’ point (SU3), with the idea of developing the experimental analyses which might be performed after the first year or so of data taking. Some benchmark points require somewhat larger datasets in order to perform kinematic measurements; as an example we show a measurement of the dilepton mass edges for the ‘‘Coannihilation’’ point (SU1) with a dataset corresponding to 18 fb^{-1} .

In sections 3 and 4 we study the decay chain:

$$\tilde{q}_L \rightarrow \tilde{\chi}_2^0 q (\rightarrow \tilde{\ell}^\pm \ell^\mp q) \rightarrow \tilde{\chi}_1^0 \ell^+ \ell^- q \quad (1)$$

in events containing two opposite-sign isolated electrons or muons, hard jets and missing energy. Kinematic endpoints in the invariant mass spectra of lepton pairs and lepton+jet combinations are fitted and used to derive relations between the masses of sparticles. In the case of first- and second-generation squarks, it will often not be possible to experimentally determine squark flavour, so we define $m_{\tilde{q}_L}$ to be the average of the masses of the \tilde{u}_L and \tilde{d}_L squarks, and $m_{\tilde{q}_R}$, the average mass of \tilde{u}_R and \tilde{d}_R .

Events with tau leptons in the final state are studied in Section 5 and di-tau mass edges in the $\tilde{\chi}_2^0$ decay chain reconstructed. This signature is particularly important in the co-annihilation region where the decay into tau stau pairs is favoured.

In Section 6 we analyse events with two hard jets and missing energy in order to measure the jet ‘‘transverse mass’’. This variable is sensitive to the mass of the right-handed squark in events where a pair of squarks are produced, each decaying as:

$$\tilde{q}_R \rightarrow q \tilde{\chi}_1^0 \quad (2)$$

A kinematical edge depending on the mass of the light stop is reconstructed in Section 7 by exploiting the decay:

$$\tilde{g} \rightarrow \tilde{t}_1 t \rightarrow \tilde{\chi}_1^\pm b t \quad (3)$$

and reconstructing the tb invariant mass.

The reconstruction of the lightest Higgs bosons, produced by the $\tilde{\chi}_2^0$ decay followed by the Higgs decay into a pair of b quarks, is investigated in Section 8. Simulations of the ‘‘Higgs’’ point (SU9) show that if these decays are allowed, then the Standard Model Higgs boson may be initially detected as a SUSY decay product rather than by signatures that involve its production via Standard Model processes.

In Section 9 the parameters measured in sections 3 to 8 are combined to extract information about the SUSY model such as the sparticle mass spectrum and the mSUGRA parameters (under the hypothesis that mSUGRA is realised).

All of these studies use a realistic detector geometry with residual misalignments, and all relevant Standard Model backgrounds are taken into account, as are the trigger efficiencies. The reconstruction of final state objects, the event selection criteria, the strategy used to simulate both signal and background events, and the methods for estimating systematic uncertainties are common across all SUSY analyses and are discussed in the introduction to this chapter [2].

2 Measurement of endpoints

The decay chain in Eq. (1) is particularly suited to measure the mass of SUSY particles, as the presence in the final state of charged leptons, missing energy from the escaping neutralino and hadronic jets ensures a large signal to background ratio. Thus, fit results are not very dependent on the precise measurement of the Standard Model background. Although we discuss the reconstruction of edges and thresholds within the mSUGRA framework, the same methodology can be applied to the large variety of SUSY models where the \tilde{q}_L decay channel in Eq. (1) is open. In the following we indicate with ℓ only electrons and muons (with $\tilde{\ell}$ being their superpartners) while τ leptons are indicated explicitly.

The endpoint in the di-lepton invariant mass distribution is a function of the masses of the particles involved in the decay. If the sleptons are heavier than the $\tilde{\chi}_2^0$ then the decay proceeds through the three body channel $\tilde{\chi}_2^0 \rightarrow \tilde{\chi}_1^0 \ell^+ \ell^-$ as in the SU4 model. In this case, the distribution of the invariant mass of the two leptons has a non-triangular shape described in [4, 5] with an endpoint equal to the difference of the mass of the two neutralinos:

$$m_{\ell\ell}^{\text{edge}} = m_{\tilde{\chi}_2^0} - m_{\tilde{\chi}_1^0} \quad (4)$$

If at least one of the sleptons is lighter than the $\tilde{\chi}_2^0$ then the two-body decay channel $\tilde{\chi}_2^0 \rightarrow \tilde{\ell}^\pm \ell^\mp \rightarrow \tilde{\chi}_1^0 \ell^+ \ell^-$ dominates. The distribution of the invariant mass of the two leptons is triangular with an endpoint at:

$$m_{\ell\ell}^{\text{edge}} = m_{\tilde{\chi}_2^0} \sqrt{1 - \left(\frac{m_{\tilde{\ell}}}{m_{\tilde{\chi}_2^0}}\right)^2} \sqrt{1 - \left(\frac{m_{\tilde{\chi}_1^0}}{m_{\tilde{\ell}}}\right)^2}. \quad (5)$$

For the SU3 point, where the $\tilde{\ell}_R$ and the $\tilde{\tau}_1$ are lighter than the $\tilde{\chi}_2^0$, such an endpoint is expected in the $\ell^+ \ell^-$ ($\tau^+ \tau^-$) distribution for $m_{\ell\ell}^{\text{edge}} = 100.2$ GeV ($m_{\tau\tau}^{\text{edge}} = 98.3$ GeV). For the SU1 point both $\tilde{\ell}_R$ and $\tilde{\ell}_L$ as well as $\tilde{\tau}_1$ and $\tilde{\tau}_2$ are lighter than $\tilde{\chi}_2^0$, resulting in a double triangular distribution for the dilepton invariant mass with two edges.

Measuring the dilepton endpoint allows us to establish a relationship between the masses of the two lightest neutralinos and any sleptons that are lighter than the $\tilde{\chi}_2^0$. For a determination of the masses of all the particles involved in the decay chain Eq. (1), further mass distributions involving a jet are used: $m_{\ell\ell q}$, $m_{\ell\ell q}^{\text{thr}}$, $m_{\ell q(\text{low})}$ and $m_{\ell q(\text{high})}$. Since it is not possible to identify the quark from the \tilde{q}_L decay, we make the assumption that it generates one of the two highest p_T jets in the event, as is normally the case if the \tilde{q}_L is much heavier than the $\tilde{\chi}_2^0$. Hence only the two leading jets are considered. For the $m_{\ell\ell q}$ distribution a maximum value of the distribution is expected so the jet giving the lowest $m_{\ell\ell q}$ value is

used. The $m_{\ell\ell q}^{\text{thr}}$ distribution is defined by the additional constraint $m_{\ell\ell} > m_{\ell\ell}^{\text{edge}}/\sqrt{2}$, giving a non-zero threshold value [6, 7]. Since a minimum is sought, the jet giving the highest $m_{\ell\ell q}$ value is used in this distribution. The distributions $m_{\ell q(\text{low})}$ and $m_{\ell q(\text{high})}$ are formed from the lower and higher m_{lq} value of each event using the same jet as for $m_{\ell\ell q}$. Both distributions have well-defined endpoints.

The theoretical values of the kinematic threshold and endpoints listed above can be calculated using the analytical expressions given in [6, 7]. The theoretical positions of the end points for the SU1, SU3 and SU4 models are summarised in Table 1.

Table 1: Value of the end points of the invariant mass distributions for the three benchmark points considered in this section. For SU1 the two endpoints correspond to the two available decay chains of the $\tilde{\chi}_2^0$ involving a right or left slepton.

Mass Distribution	SU1 end point (GeV)	SU3 end point (GeV)	SU4 end point (GeV)
$m_{\ell\ell}^{\text{edge}}$	56.1, 97.9	100.2	53.6
$m_{\tau\tau}^{\text{edge}}$	77.7, 49.8	98.3	53.6
$m_{\ell\ell q}^{\text{edge}}$	611, 611	501	340
$m_{\ell\ell q}^{\text{thr}}$	133, 235	249	168
$m_{lq(\text{low})}^{\text{max}}$	180, 298	325	240
$m_{lq(\text{high})}^{\text{max}}$	604, 581	418	340

Another advantage of the decay chain in 1 is the possibility of estimating both the SUSY combinatorial background and the Standard Model background from the data with high accuracy. The technique, known as *flavour subtraction*, is based on the fact that the signal contains two opposite-sign same-flavour (OSSF) leptons, while the background leptons come from different decay chains, which can be of the same flavour or of different flavour with the same probability. The background thus cancels in the subtraction:

$$N(e^+e^-)/\beta + \beta N(\mu^+\mu^-) - N(e^\pm\mu^\mp) \quad (6)$$

where $\beta = 0.86$ is an efficiency correction factor equal to the ratio of the electron and muon reconstruction efficiencies. The value of β is taken from [8, 9], and is assumed in the following to be known with an uncertainty of 10%.

3 Dilepton edges

3.1 Event Selection

Events with two or three isolated leptons (electrons or muons) with $p_T > 10$ GeV and $|\eta| < 2.5$ are selected. If two leptons are selected, they are required to have opposite signs. If three leptons are present, the two opposite-sign combinations are considered and treated independently in the rest of the analysis.

In order to select SUSY events and reject the Standard Model background it is necessary to require the presence of energetic jets and missing energy. The variables used to discriminate SUSY from the SM background are the transverse missing energy, the transverse momenta of the four leading jets, the ratio between the transverse missing energy and the effective mass, and the transverse sphericity (S_T). In order to optimise the cuts on these variables, the value of:

$$S \equiv (N_{\text{OSSF}} - N_{\text{OSDF}})/\sqrt{N_{\text{OSSF}} + N_{\text{OSDF}}} \quad (7)$$

is maximized for each SUSY point, where N_{OSSF} and N_{OSDF} are the number of same-flavour and different-flavour lepton pairs respectively.

The S variable can be computed from collider data, since no Monte Carlo information is used. By maximizing the value of S we are maximizing the selection efficiency for signal events while suppressing the Standard Model and the SUSY combinatorial backgrounds.

In order to improve the sensitivity to the signal, only lepton pairs with an invariant mass $m_{\ell\ell} < m_{\ell\ell}^{\text{edge}} + 10$ GeV are considered. Since the true value of the endpoint is *a priori* unknown, this choice implies that the edge has already been observed, and that afterwards the selection cuts are optimised as described here in order to improve the separation between signal and background and the measurement of the endpoint. We are thus focusing here on determining selection cuts that would allow a precise measurement of the endpoint with moderate statistics, rather than on finding the first evidence for an excess of different-flavour lepton pairs or the first evidence for the presence of the edge.

In Table 2 the optimal selection resulting from the scan is shown. For all three points a 2-jet selection is preferred, leaving out cuts on the third and fourth jets, on S_{T} and on the ratio $E_{\text{T}}^{\text{miss}}/M_{\text{eff}}$. For the ‘‘Coannihilation’’ point (SU1) and the ‘‘Bulk’’ point (SU3) the S -value is found to be stable in an interval around the maximum value. For the ‘‘Low Mass’’ point (SU4) the best S -value is found for the loosest cut allowed by the available Monte Carlo samples. Hence even looser cuts may be preferred as far as the value of S is concerned. The cuts on $E_{\text{T}}^{\text{miss}}$ and the p_{T} of leading jet are however required in order to have a high trigger efficiency²⁾.

Table 2: Results of the event-selection optimisation for the S -variable Eq. (7) for signal (s) and Standard Model background (b) with range limit $m_{\ell\ell} < m_{\ell\ell}^{\text{edge}} + 10$ GeV, for SU1, SU3 and SU4 for 1 fb^{-1} . The best selection is shown.

	p_{T}^{j1}	p_{T}^{j2}	p_{T}^{j3}	p_{T}^{j4}	$E_{\text{T}}^{\text{miss}}$	$E_{\text{T}}^{\text{miss}}/M_{\text{eff}}$	S_{T}	s_{OSSF}	s_{OSDF}	b_{OSSF}	b_{OSDF}	S
SU1	200	150	-	-	120	-	-	120	64	69	53	5.1
SU3	180	100	-	-	120	-	-	615	149	93	92	15.1
SU4	100	50	-	-	100	-	-	3048	1574	411	419	19.9

The number of signal and background lepton pairs passing the selection cuts is shown in Table 3. All numbers are for 1 fb^{-1} . The main Standard Model background is always $t\bar{t}$ accounting for about 95% of the total background. The remaining background events are from W, Z and WW, WZ, ZZ production. The background due to QCD jets is negligible. The fraction of SUSY events in the selected sample with OSSF leptons is 59% for SU1, 77% for SU3, and 80% for SU4.

3.2 Reconstruction of the dilepton edge

The distribution of the invariant mass of same-flavour and different-flavour lepton pairs is shown in Fig. 1 for the SUSY benchmark points and backgrounds, after the selection cuts optimized for SU3 (left plot) and SU4 (right plot), and for an integrated luminosity of 1 fb^{-1} and 0.5 fb^{-1} respectively. It can be seen from regions where the signal does not contribute (i.e. for the Standard Model backgrounds and for $m_{\ell\ell} > m_{\ell\ell}^{\text{edge}}$ for SUSY) that the different-flavour distributions are similar to the same-flavour backgrounds.

²⁾For this channel, both the lepton triggers and the trigger based on $E_{\text{T}}^{\text{miss}}$ may be relied upon. The latter are however less efficient, and they would imply different p_{T} thresholds for electrons and muons.

Table 3: Number of lepton pairs passing the selection cuts optimized for the SUSY sample SU1 (above), SU3 (middle) and SU4 (below), for 1 fb^{-1} of integrated luminosity. The contribution from $t\bar{t}$ production is indicated separately as it constitutes most of the Standard Model background. The remaining background events are from W, Z and WW, WZ, ZZ production. The background due to QCD jets is negligible.

Sample	e^+e^-	$\mu^+\mu^-$	OSSF	OSDF
SUSY SU1	56	88	144	84
Standard Model ($t\bar{t}$)	35 (35)	65 (63)	101 (99)	72 (68)
SUSY SU3	274	371	645	178
Standard Model ($t\bar{t}$)	76 (75)	120 (115)	196 (190)	172 (165)
SUSY SU4	1729	2670	4400	2856
Standard Model ($t\bar{t}$)	392 (377)	688 (657)	1081 (1035)	1104 (1063)

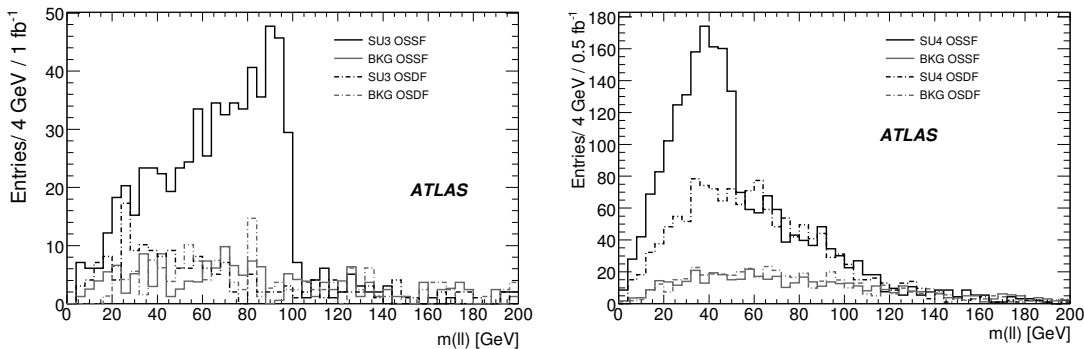


Figure 1: Left: distribution of the invariant mass of same-flavour and different-flavour lepton pairs for the SUSY benchmark points and backgrounds after the cuts optimized from data in presence of the SU3 signal (left), and the SU4 signal (right). The integrated luminosities are 1 fb^{-1} and 0.5 fb^{-1} respectively.

The invariant mass distribution after flavour subtraction is shown in the left plot of Fig. 2 in the presence of the SU3 signal and for an integrated luminosity of 1 fb^{-1} . The distribution has been fitted with a triangle smeared with a Gaussian. The value obtained for the endpoint is $(99.7 \pm 1.4 \pm 0.3) \text{ GeV}$ where the first error is due to statistics and the second is the systematic error on the lepton energy scale and on the β parameter [2]. This result is consistent with the true value of 100.2 GeV calculated from Eq. (5).

The right plot of Fig. 2 shows the flavour-subtracted distribution in the presence of the SU4 signal for an integrated luminosity of 0.5 fb^{-1} . The fit was performed using the function from [5] which describes the theoretical distribution for the 3-body decay in the limit of large slepton masses, smeared for the experimental resolution. This function vanishes near the endpoint and is a better description of the true distribution for SU4 than the triangle with a sharp edge. The endpoint from the fit is $(52.7 \pm 2.4 \pm 0.2) \text{ GeV}$, consistent with the theoretical endpoint of 53.6 GeV .

Since the true distribution will not be known for data, the distribution was also fitted with the smeared triangle expected for the 2-body decay chain. This also gives a good χ^2 with an endpoint of $(49.1 \pm 1.5 \pm 0.2) \text{ GeV}$. A larger integrated luminosity will be required to use the shape of the distribution to discriminate between the two-body and the three-body decays.

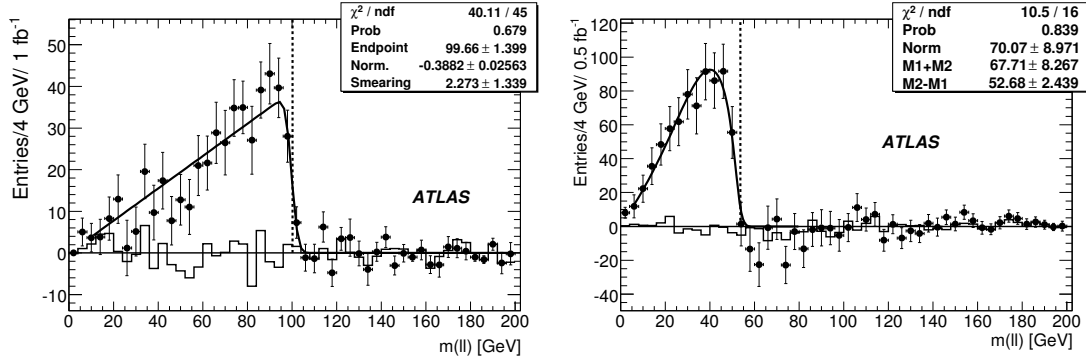


Figure 2: Left: Distribution of invariant mass after flavour subtraction for the SU3 benchmark point with an integrated luminosity of 1 fb^{-1} . Right: the same distribution is shown for the SU4 benchmark point and an integrated luminosity of 0.5 fb^{-1} . The line histogram is the Standard Model contribution, while the points are the sum of Standard Model and SUSY contributions. The fitting function is superimposed and the expected position of the endpoint is indicated by a dashed line.

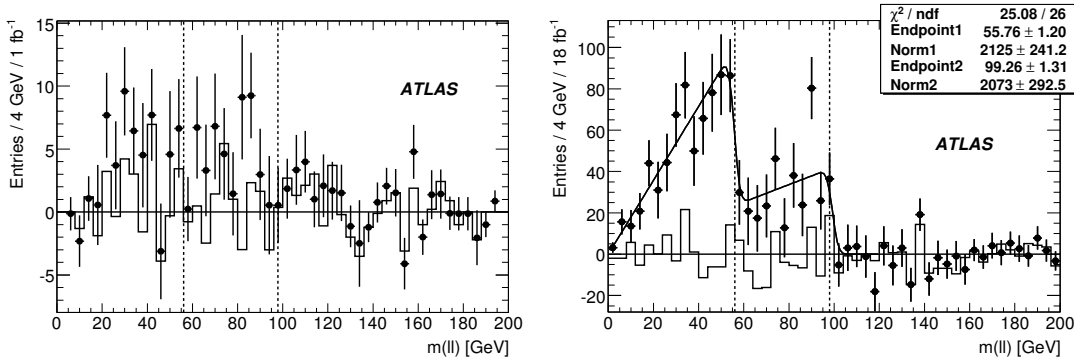


Figure 3: Distribution of invariant mass after flavour subtraction for the SU1 point and for an integrated luminosity of 1 fb^{-1} (left) and 18 fb^{-1} (right). The points with error bars show SUSY plus Standard Model, the solid histogram shows the Standard Model contribution alone. The fitted function is superimposed (right), the vertical lines indicate the theoretical endpoint values.

In Fig. 3 the flavour-subtracted distribution of the dilepton mass is shown for the SU1 point at an integrated luminosity of 1 fb^{-1} (left) and 18 fb^{-1} (right)³⁾. While there is already a clear excess of SF-OF entries at 1 fb^{-1} , a very convincing edge structure cannot be located. At 18 fb^{-1} the two edges are visible. A fit function consisting of a double triangle convoluted with a Gaussian, the latter having a fixed width of 2 GeV, returns endpoint values of $55.8 \pm 1.2 \pm 0.2 \text{ GeV}$ for the lower edge and $99.3 \pm 1.3 \pm 0.3 \text{ GeV}$ for the upper edge, consistent with the true values of 56.1 and 97.9 GeV. As can be seen from Fig. 3 (right) the $m_{\ell\ell}$ distribution also contains a noticeable contribution from the leptonic decay of Z bosons present in SUSY events. Even though the upper edge is located close to the Z mass,

³⁾Only 1 fb^{-1} of simulated Standard Model background was available. To scale the Standard Model contribution to higher luminosities a probability density function for the $m(\text{ll})$ distribution was constructed by fitting a Landau function to the 1 fb^{-1} distribution, assuming statistically identical shapes for e^+e^- , $\mu^+\mu^-$ and $e^\pm\mu^\mp$ and normalisation according to a β of 0.86. The systematic uncertainty on the endpoint determination from this procedure was estimated to be a small fraction of the statistical uncertainty.

adding a Z peak of fixed mass and width to the fit function only affects the endpoints at the 0.2-0.3 GeV level. However the Z peak changes the normalisation of the upper triangle so for considerations of couplings and branching ratios it should be included.

4 Leptons+Jets edges

In events selected for the dilepton analysis in the previous section, jets are added to construct further distributions as described in Sect. 2. Additional selection cuts are applied to refine the distributions:

$$m_{\ell\ell} < m_{\ell\ell}^{\text{edge}} + \Delta_1 \quad (\text{all distributions}) \quad (8)$$

$$m_{\ell\ell q} < m_{\ell\ell q}^{\text{edge}} + \Delta_2 \quad (m_{\ell q} \text{ distributions}) \quad (9)$$

Here $m_{\ell\ell}^{\text{edge}}$ and $m_{\ell\ell q}^{\text{edge}}$ refer to experimental values found in this and the previous section. The value Δ_1 is a small number, 10 (3.3) GeV for SU3 (SU4), to account for the fact that the edge stretches slightly beyond the fitted endpoint. One can see from Fig. 1 that this cut should be very effective for SU4, but much less so for SU3. The value Δ_2 serves a similar purpose, but since the determination of $m_{\ell\ell q}^{\text{edge}}$ is less reliable, a looser cut is used, 155 (37) GeV for SU3 (SU4).

The invariant mass distributions $m_{\ell\ell q}$ and $m_{\ell q}$ are shown in Figures 4 and 5 for both the ‘‘Bulk’’ point (SU3) and the ‘‘Low Mass’’ point (SU4) after efficiency-corrected flavour subtraction.

While the Standard Model background causes considerable bin-by-bin fluctuations for integrated luminosities $\lesssim 1 \text{ fb}^{-1}$, the net contribution of entries beyond the endpoints is mainly due to combinatorics from choosing the wrong jet in a true SUSY event. For the distributions where a clear tail is visible, a straight line is assumed for the background, otherwise it is set to zero. (The statistics box of the plots indicates which background hypothesis is used.) Since the tail is due to SUSY events, it will not be known beforehand and a data-driven approach (not described here) would be required.

The lepton+jet distributions have shapes which depend on the sparticle masses [10]. Depending on the sparticle spectrum, the edge region may contain non-trivial features such as experimentally undetectable ‘feet’ containing very few events or vertical drops. For all the relevant distributions of two-body scenarios, analytic formulas describing the shape in terms of the sparticle masses are known [11, 12]. With low statistics a straight-line fit is likely to give a sufficiently good description in many cases. All the edges and thresholds were fitted with the following formula,

$$f(m) = \frac{1}{\sqrt{2\pi}\sigma} \int \exp\left(-\frac{(m-m')^2}{2\sigma^2}\right) \max\{A(m'-m^{\text{EP}}), 0\} dm' + \max\{a+bm, 0\}, \quad (10)$$

where m^{EP} represents the endpoint (or threshold), A is the slope of the signal distribution, while a and b are the background parameters. The Gaussian smearing gives a smooth transition between the two straight lines and mimics in a simple way the smearing of an edge due to mismeasurement of jet momenta. The smearing parameter σ was fixed to 15 GeV. The fitted endpoint values were found not to be very sensitive to the choice of σ in the range 0–20 GeV. For $m_{\ell\ell q}$ and the $m_{\ell q}$ distributions the integration range is $(0, m^{\text{EP}})$. For the $m_{\ell\ell q}^{\text{thr}}$ distribution the lower integration limit is m^{EP} while some 100–200 GeV above the upper fit range is a safe upper integration limit. The endpoints resulting from the fits to the distributions in Figures 4 and 5 are summarised in Table 4.

For the ‘‘Bulk’’ point (SU3) the edges are found to be sufficiently well described by a straight line in Eq. (10) for the signal region, however describing the background region by a straight line results in large systematic uncertainties in the endpoint fit. In particular, the $m_{\ell\ell q}$ distribution does not have a clear edge. Even though the $m_{\ell\ell q}$ cut in Eq. (9) removes a considerable amount of background for the $m_{\ell q(\text{low})}$ distribution there is still some background left for the $m_{\ell q(\text{high})}$ distribution. A systematic uncertainty is assigned to account for the background estimation for both fits. In case of $m_{\ell q(\text{low})}$ a background-free fit

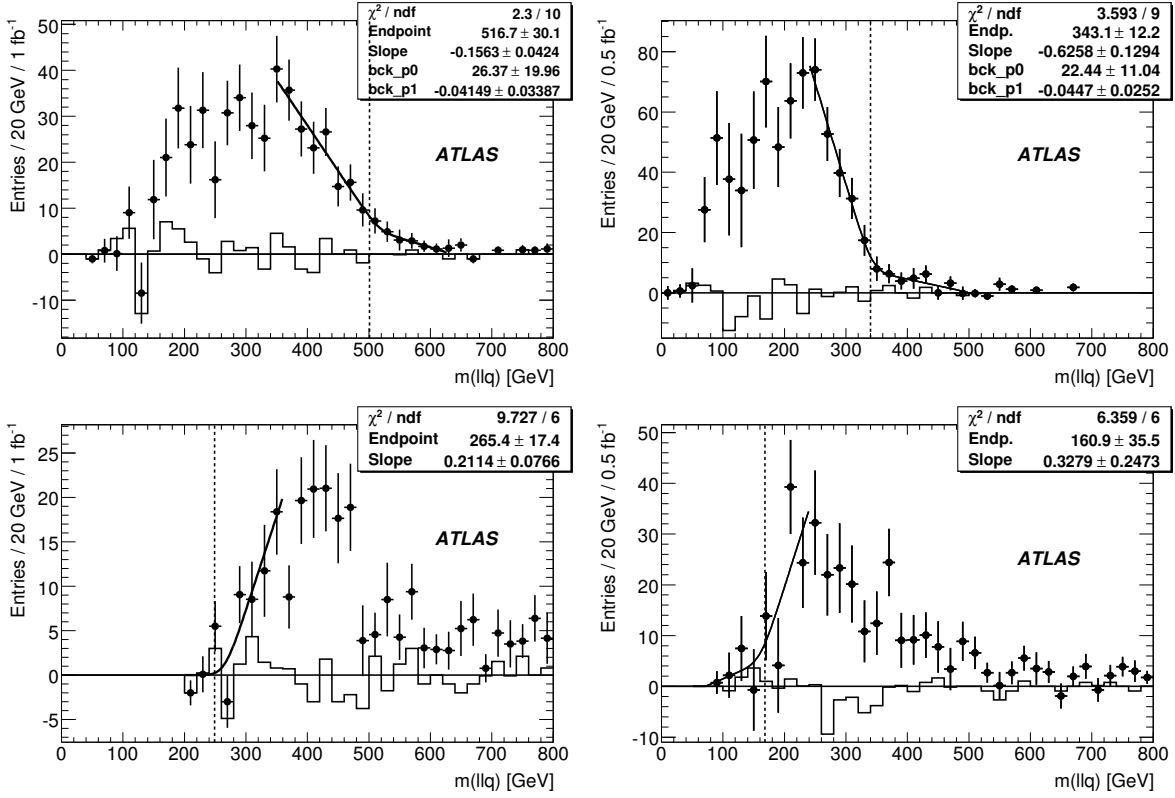


Figure 4: Efficiency-corrected flavour-subtracted distributions of $m_{\ell\ell q}$ (top) and $m_{\ell\ell q}^{\text{thr}}$ (bottom) for SU3 (left) for 1 fb^{-1} and SU4 (right) with 0.5 fb^{-1} of integrated luminosity. The points with error bars show SUSY plus Standard Model, the solid histogram shows the Standard Model contribution alone. The fitted function is superimposed, the vertical line indicates the theoretical endpoint value.

can be made resulting in a few GeV uncertainty. The $m_{\ell\ell q}^{\text{thr}}$ distribution is expected to be concave, so a systematic uncertainty is added in the estimation when fitting the threshold by a straight line fit.

For SU4, the $m_{\ell\ell q}$ and both of the $m_{\ell q}$ distributions have edges which are well described by the fit function Eq. (10). This is confirmed by the dominance of the statistical errors over the systematics ones. The $m_{\ell\ell q}^{\text{thr}}$ fit is more problematic resulting in somewhat larger errors. This could be expected since the contributions from different-family and non-signal same-family peaks in this mass region, whereas they are close to vanishing in the edge regions of the other distributions. Another reason (although probably of less importance at 0.5 fb^{-1}) is that the threshold edge is concave and only moderately well described by a straight line.

While the fit values of $m_{\ell\ell q}^{\text{edge}}$ and $m_{\ell\ell q}^{\text{thr}}$ are compatible with the theoretical values, the fitted $m_{\ell q(\text{high})}^{\text{max}}$ and $m_{\ell q(\text{low})}^{\text{max}}$ are off by 2σ and 4σ , respectively. This comes from the fact that in SU4 the decay of $\tilde{\chi}_2^0$ is a three-body decay. In such scenarios the $m_{\ell q}$ distributions, and in particular $m_{\ell q(\text{low})}$ are often so sparsely populated towards the high mass values that the endpoints are not experimentally deducible from the edges. Note, however, that there is no hint from the χ^2 of the $m_{\ell q(\text{low})}$ fit that we are in such a situation. This topic is discussed further in Sect. 9.1 where endpoint relations are inverted to give sparticle masses.

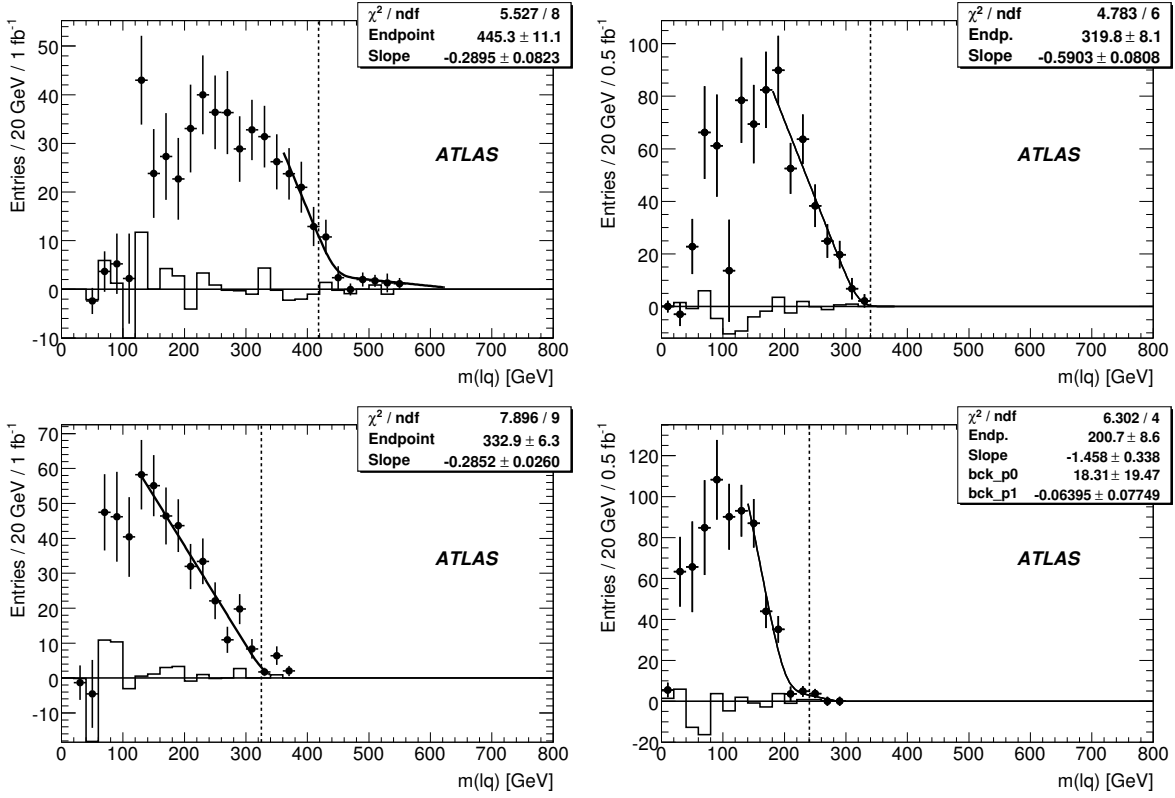


Figure 5: Efficiency-corrected flavour-subtracted distributions of $m_{lq(\text{high})}$ (top) and $m_{lq(\text{low})}$ (bottom) for SU3 (left) with 1 fb⁻¹ and SU4 (right) with 0.5 fb⁻¹ of integrated luminosity. The points with error bars show SUSY plus Standard Model, the solid histogram shows the Standard Model contribution alone. The fitted function is superimposed, the vertical line indicates the theoretical endpoint value.

5 Tau signatures

5.1 Determination of the di-tau endpoint position

The endpoint of the invariant mass distribution from two taus emerging from a $\tilde{\chi}_2^0$ decay,

$$\tilde{\chi}_2^0 \rightarrow \tilde{\tau}_1 \tau \rightarrow \tilde{\chi}_1^0 \tau^\pm \tau^\mp, \quad (11)$$

depends on the masses of the $\tilde{\chi}_2^0$, the $\tilde{\chi}_1^0$ and the $\tilde{\tau}_1$, and therefore can contribute to the determination of SUSY parameters.

Taus play an important role in scenarios like mSUGRA where $\tilde{\chi}_2^0$ is mostly wino, and therefore preferentially couples to L -type sfermions. The large L - R mixing in the stau sector significantly enhances the branching ratio for the decay $\tilde{\chi}_2^0 \rightarrow \tilde{\tau}_1^\pm \tau^\mp$ with respect to other leptons. In the scenarios SU1 and SU3 studied here, for example, the branching ratio for the decays into taus is a factor of 10 larger than for decays into electrons or muons. Since in many models (including mSUGRA) the $\tilde{\tau}_1$ is the lightest slepton, for certain values of the SUSY parameters the only allowed two body decay is $\tilde{\chi}_2^0 \rightarrow \tilde{\tau} \tau$ as $\tilde{\chi}_2^0 \rightarrow \tilde{\chi}_1^0 h$, $\tilde{\chi}_2^0 \rightarrow \tilde{\chi}_1^0 Z$, and $\tilde{\chi}_2^0 \rightarrow \tilde{e} e$ or $\tilde{\mu} \mu$ are kinematically forbidden.

Finally, whereas mass information about $\tilde{\chi}_1^0$ and $\tilde{\chi}_2^0$ can often be obtained more precisely from $\tilde{\chi}_2^0$ decays into electrons and muons (if these decays are open), decays into taus are needed to probe the $\tilde{\tau}$ mass parameters.

Table 4: Endpoint positions for SU3 and SU4, in GeV. The first error is statistical, the second and third are the systematic and the jet energy scale uncertainty, respectively. The theoretical values are also given for ease of comparison to the left of the fitted values. The integrated luminosity assumed is 1 fb^{-1} for SU3 and 0.5 fb^{-1} for SU4.

Endpoint	SU3 truth	SU3 measured	SU4 truth	SU4 measured
$m_{\ell\ell q}^{\text{edge}}$	501	$517 \pm 30 \pm 10 \pm 13$	340	$343 \pm 12 \pm 3 \pm 9$
$m_{\ell\ell q}^{\text{thr}}$	249	$265 \pm 17 \pm 15 \pm 7$	168	$161 \pm 36 \pm 20 \pm 4$
$m_{lq(\text{low})}^{\text{max}}$	325	$333 \pm 6 \pm 6 \pm 8$	240	$201 \pm 9 \pm 3 \pm 5$
$m_{lq(\text{high})}^{\text{max}}$	418	$445 \pm 11 \pm 11 \pm 11$	340	$320 \pm 8 \pm 3 \pm 8$

In contrast to $\tilde{\chi}_2^0$ decays into electrons or muons, the di-tau invariant mass spectrum does not have a sharp endpoint at the maximum kinematic value. Due to the presence of neutrinos from the tau decays, the $m_{\tau\tau}$ distribution (where $m_{\tau\tau}$ indicates the invariant mass of the visible decay products of the tau pair) falls off smoothly below the maximum value given by either Eq. (4) or Eq. (5). Only hadronic tau decays are considered for tau identification: the tracking-seeded reconstruction algorithm [13] is used to reconstruct taus in the ‘‘Coannihilation’’ point (SU1), while the calorimeter-seeded algorithm [13] is used for the ‘‘Bulk’’ point model (SU3). This choice is motivated by the higher efficiency of the former in reconstructing the low p_T taus that are present in the SU1 model.

The SU1 point also has a considerably lower cross-section than the SU3 point, so different selection procedures are used to maximize the signal significance. For the SU3 point events are selected with two taus, $E_T^{\text{miss}} > 230 \text{ GeV}$, and at least four jets with p_T greater than 220, 50, 50, 30 GeV respectively. For the SU1 point the cut on E_T^{miss} is relaxed to 100 GeV and at least two jets with p_T greater than 100 and 50 GeV respectively. In addition, an elliptical cut in the space of E_T^{miss} and the sum $p_T(1) + p_T(2)$ of the two highest p_T jets is applied to SU1. The semi-axes of the ellipse are 450 GeV for E_T^{miss} and 500 GeV for the sum of jet p_T . This cut exploits the anticorrelation between E_T^{miss} and $(p_T(1) + p_T(2))$ which is different for the signal and the Standard Model background.

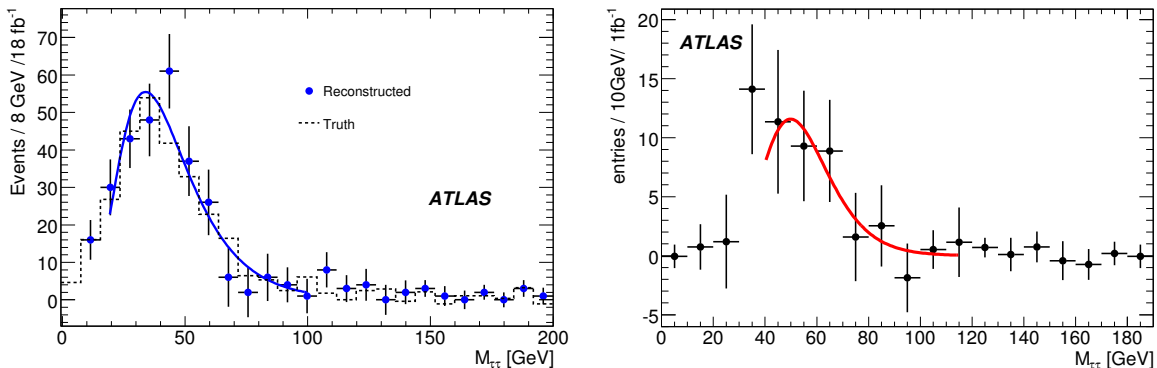


Figure 6: Invariant mass distribution of opposite-sign tau pairs with same-sign tau distribution subtracted, for the SU1 (18 fb^{-1} , left) and SU3 scenarios (1 fb^{-1} , right). The dashed histogram in the left plot shows the distribution at the generator level, while points show the reconstruction-level distribution.

The invariant mass distribution emerging after the above cuts are applied is shown in Figure 6 for the SU1 and SU3 scenarios, where the corresponding distribution of two taus with the same sign of electric

charge is subtracted from tau pairs with opposite sign in order to reduce combinatorial background. This is possible because uncorrelated and fake taus should arise about as often with the same charge as with opposite charges. To decrease the SUSY background further, the two taus arising from the same decay chain are required to have a maximum separation $\Delta R < 2$ in the η - ϕ -plane.

The following log normal function with three parameters, inspired by [14], is used to fit the $m_{\tau\tau}$ distribution:

$$f(x) = \frac{p_0}{x} \cdot \exp\left(-\frac{1}{2p_2^2}(\ln(x) - p_1)^2\right) \quad (12)$$

This function does not contain the endpoint position explicitly, but approaches the x-axis asymptotically. The endpoint is then derived from the inflection point m_{IP} of the fit function:

$$m_{IP} = \exp\left(-\frac{1}{2}p_2^2\left(3 - \sqrt{1 + \frac{4}{p_2^2}}\right) + p_1\right) \quad (13)$$

using a Monte Carlo-based calibration procedure.

The inflection point obtained for 14 SU3-like models is plotted against the theoretical endpoint value for each of these models. The SU3-like points are generated using the ATLAS fast simulation program [15] and varying the masses of the $\tilde{\chi}_2^0$, the $\tilde{\tau}_1$ and the $\tilde{\chi}_1^0$ separately, while keeping the other two masses fixed. In Figure 7 the inflection point is plotted as a function of the endpoint m_{EP} and fitted with a straight line, yielding the following calibration function:

$$m_{IP} = (0.47 \pm 0.02)m_{EP} + (15 \pm 2) \text{ GeV} \quad (14)$$

The covariance between the slope and the axis intercept is -0.034 GeV.

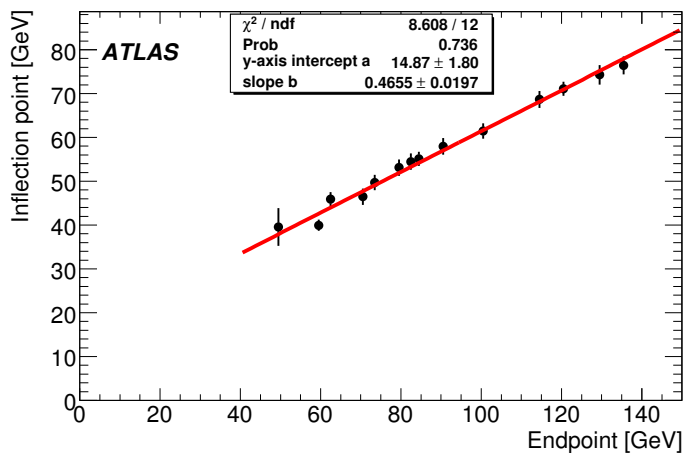


Figure 7: Calibration curve showing the relation between the position of the inflection point (measured and fitted with function Eq. (12) after ATLFAST based detector simulation) and the endpoint (calculated with equation Eq. (5)) of the di-tau mass distribution. The SU3 point is not included.

The fit using function Eq. (12) for the SU1 and SU3 models is shown in Fig. 6 giving an inflection point at $m_{IP} = 48 \pm 3$ GeV and $m_{IP} = 62 \pm 8$ GeV respectively, which translates into endpoints at $m_{EP} = (70 \pm 6.5^{\text{stat}} \pm 5^{\text{syst}})$ GeV (SU1) and $(102 \pm 17^{\text{stat}} \pm 5.5^{\text{syst}})$ GeV (SU3) using the calibration relation in Eq. (14). The systematic uncertainty is dominated by the fitting procedure and is evaluated by changing the binning and fit ranges. The effects of 1% and 5% jet energy scale uncertainties have been tested and

found to introduce an additional systematic uncertainty on the endpoint measurement well below 3%, so they are negligible compared to the systematic error introduced by the fitting procedure. The theoretical expectation for the SU1 (SU3) endpoint is 78 GeV (98 GeV). The difference between the theoretical and the extracted endpoint comes from the fitting and fit-calibration procedure rather than from detector effects. As Fig. 6 (left) shows, the generator-level distribution of the visible products is close to the reconstruction-level distribution and after fitting gives an endpoint value of 70 GeV for the SU1 scenario which is the same as for the reconstructed distribution.

5.2 Impact of the tau polarization on the di-tau mass spectrum

The method discussed in the previous section assumes a fixed polarization of the two taus from the $\tilde{\chi}_2^0$ and therefore neglects the effect of the polarization on the invariant mass spectra. However, the polarization of the taus from the decay cascade can vary significantly between different SUSY models. Polarization effects on the di-tau mass distribution are studied by simulating samples of events where the polarization of the two taus from the decay Eq. (11) is allowed to vary. The ATLAS fast simulation program [15] is used to simulate a data sample equivalent to 51 fb^{-1} of data.

Parity violation in weak interactions in conjunction with momentum and angular momentum conservation leads to a correlation between the visible tau energy and the polarization of the tau. In case of the decay $\tau \rightarrow \nu_\tau \pi^-$, since the pion is a scalar particle the neutrino spin is forced to be parallel to that of the tau and therefore the fixed neutrino helicity determines the neutrino momentum direction. Thus, to conserve momentum, the direction of the pion momentum is forced to be parallel or antiparallel to that of the tau depending on the tau polarization. This leads to the pion getting a boost parallel or antiparallel to the tau momentum resulting in harder and softer pions. This affects the di-tau mass spectrum, as shown in Fig. 8. The curves in the plot are theoretical predictions from [16]. The invariant masses of taus with left chirality (LL) are on average smaller than for right (RR) taus.

For decays via the vector mesons ρ and a_1 , the momentum of the vector meson has the same (opposite) direction as in the case of pions for longitudinal (transverse) polarization of the vector meson.

Adding all hadronic tau decay modes finally yields the invariant mass distributions shown in Figure 8 for the chirality options LL , RR and LR/RL . The position of the trailing edge is clearly shifted for different polarizations whereas the shape difference calculated in [16] is barely visible after detector simulation.

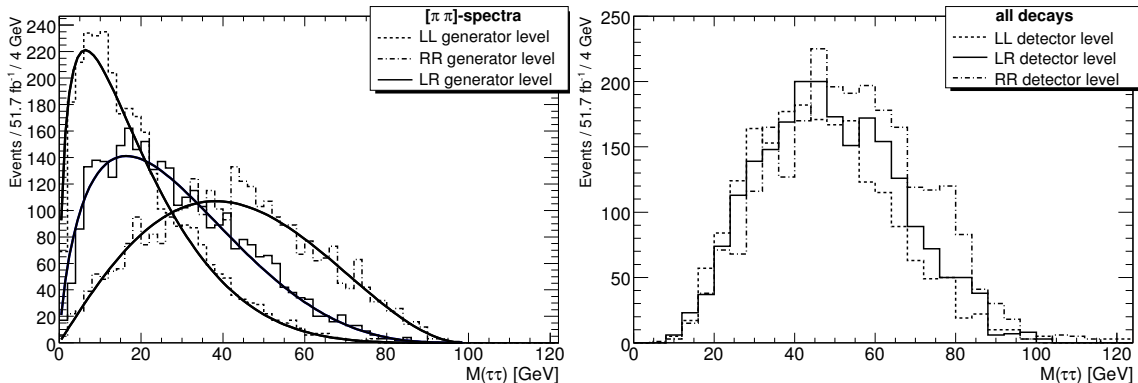


Figure 8: Left: Di-tau invariant mass spectrum for $\tau \rightarrow \pi \nu_\tau$ decays as obtained from Monte Carlo truth information together with the expectation from theory. Right: Di-tau invariant mass spectrum for all hadronic decays after an ATLFAST based detector simulation. Both plots show the mass distributions for the chirality states LL , RR and LR/RL .

As a consequence, the inflection point of the distribution is shifted due to polarization effects. The maximum difference in the inflection point measurement $\Delta m_{IPA}(RR - LL)$ has been found to be 7 GeV which is comparable to the statistical error on the position of the inflection point presented in the previous section. Without additional information on the tau polarization we might quickly reach a point where it is not possible to improve the di-tau endpoint measurement. In this case the achievable precision for an integrated luminosity of 1 fb^{-1} for the SU3 model is:

$$m_{\tau\tau}^{\text{max}} = 102 \pm 17^{\text{stat}} \pm 5.5^{\text{syst}} \pm 7^{\text{pol}}$$

The uncertainty due to the polarization effects dominates over the other systematic uncertainties and therefore needs special attention. A study of the different polarization dependencies of the decay kinematics for different decay modes of the tau might be helpful. As the emission direction of vector mesons is opposite for longitudinal and transversal states the net effect is determined by the branching ratio into the two states. It turns out that for the a_1 there are as many longitudinal as transverse polarized whereas for the ρ there are more longitudinal vector mesons, leading to different polarization dependencies.

6 \tilde{q}_R pair reconstruction

Events where a pair of \tilde{q}_R particles is produced, and where each decays through the process

$$\tilde{q}_R \rightarrow \tilde{\chi}_1^0 q \quad (15)$$

lead to a characteristic signature with two high- p_T jets and large E_T^{miss} from the escaping neutralinos. \tilde{q}_R pair production represents about 10% (5%) of the total SUSY production cross-section for the ‘‘Bulk’’ point SU3 (‘‘Low Mass’’ SU4). For both points (and more generally in most of mSUGRA parameter space) the \tilde{q}_R decays almost entirely through the process in Eq. (15).

Events with large E_T^{miss} and a pair of high- p_T jets are selected by requiring:

- $E_T^{\text{miss}} > \max(200 \text{ GeV}, 0.25M_{\text{eff}})$ and $M_{\text{eff}} > 500 \text{ GeV}$
- Two jets with $p_T > \max(200 \text{ GeV}, 0.25M_{\text{eff}})$, $|\eta| < 1$ and $\Delta R > 1$
- No additional jet with $p_T > \min(200 \text{ GeV}, 0.15M_{\text{eff}})$
- No isolated leptons and no jets tagged as b jets
- Transverse sphericity $S_T > 0.2$

These selection cuts are tuned using the information from the event generation to select \tilde{q}_R pair production.

The systematic uncertainty originating from the jet and E_T^{miss} energy scale and resolution [2] change the event yield by 7% for the case of SU3 and by 25% for the case of SU4. The systematic effect on the energy scale and resolution of leptons is negligible.

The total event yield and the number of Standard Model background events satisfying the selection criteria for 1 fb^{-1} for SU3 and 0.50 fb^{-1} for SU4 are given in Table 5 together with the signal-to-background ratio and the signal statistical significance.

To reconstruct the \tilde{q}_R mass we use the the m_{T2} variable [2, 17, 18], sometimes referred to as ‘‘straverse’’ mass. This variable uses the kinematic features of the \tilde{q}_R decays to reconstruct $m_{\tilde{q}_R}$ ⁴⁾ making the

⁴⁾For the benchmark point considered here, the effect of the SUSY background (i.e. events other than the \tilde{q}_R pair production which pass the event selection) on the position of the edge is small. This has also been shown to be true for other benchmark points [10]. However, the identification of the edge as a measurement of the \tilde{q}_R mass may not hold for all the SUSY parameter space.

Table 5: The total event yield and the number of Standard Model background events satisfying selection criteria for m_{T2} reconstruction, signal-to-background ratio and signal statistical significance. Only errors from the detector systematic uncertainties are quoted.

	Integrated luminosity (fb^{-1})	Event yield	Standard Model	S/B_{SM}	$S/\sqrt{B_{SM}}$
SU3	1.0	282 ± 20	18	14.7 ± 1.1	62.2 ± 4.7
SU4	0.5	258 ± 65	9	27.7 ± 7.2	83.0 ± 21.7

assumption that $m_{\tilde{\chi}_1^0}$ is known from the measurements in Section 4. The m_{T2} distributions for the SU3 and SU4 points are shown in Figure 9. As is common for SUSY measurements, the distribution is expected to have an edge at $m_{\tilde{q}_R}$ rather than a peak. A linear fit is applied to the right part of the distribution to determine the edge position at $590 \pm 9(\text{stat})_{-6}^{+13}(\text{sys})$ GeV for SU3 and $421 \pm 17(\text{stat})_{-3}^{+10}(\text{sys})$ GeV for SU4. This can be compared to the expected positions of $m_{\tilde{q}_R} = 611$ GeV for SU3 and $m_{\tilde{q}_R} = 406$ GeV for SU4. The systematic error accounts for the choice of the fit limits as well as the jet energy scale systematic.

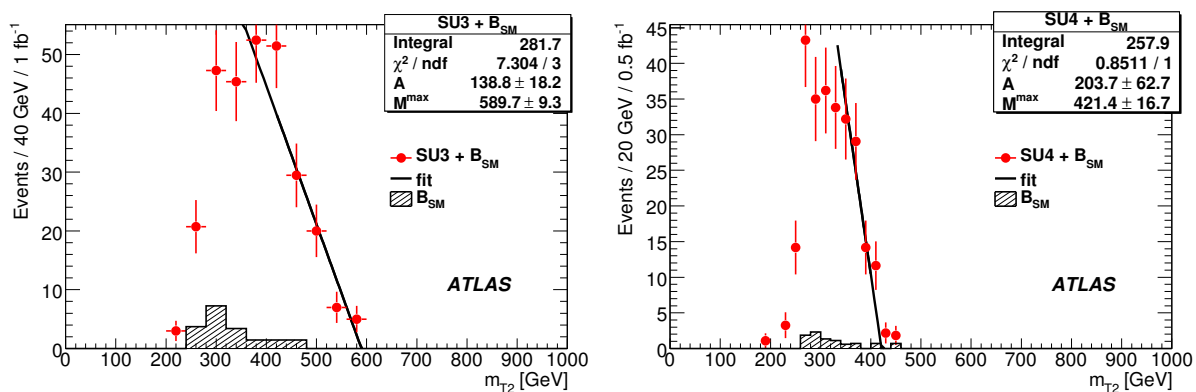


Figure 9: Fit of the sum of the reconstructed m_{T2} distributions in the selected SUSY and the remaining Standard Model background events with 1 fb^{-1} for SU3 and 0.5 fb^{-1} for SU4.

7 Light stop signature

In the “Low Mass” benchmark point (SU4), the SUSY masses are all in the range $m_{\tilde{\chi}_1^0} = 60 \text{ GeV} < m < m_{\tilde{t}_2} = 445 \text{ GeV}$. The stop \tilde{t}_1 is light ($m_{\tilde{t}_1} = 206 \text{ GeV}$) and always decays by $\tilde{t}_1 \rightarrow \tilde{\chi}_1^\pm b$. A detailed analysis of the phenomenology of this point can be found in [19].

At this SU4 benchmark point the light stop is produced in the gluino decay Eq. (3) which has a branching ratio of 42%. Associated gluino production with a \tilde{q}_L or \tilde{q}_R followed by the decay in Eq. (3) occurs in $\sim 18\%$ of all SU4 events. In the decay Eq. (3) the final state tb invariant mass distribution has the upper kinematic endpoint:

$$M^{\text{max}}(tb) = \left[m_t^2 + \frac{m_{\tilde{t}_1}^2 - m_{\tilde{\chi}_1^\pm}^2}{2m_{\tilde{t}_1}^2} \left((m_{\tilde{g}}^2 - m_{\tilde{t}_1}^2 - m_t^2) + \sqrt{(m_{\tilde{g}}^2 - (m_{\tilde{t}_1} - m_t)^2)(m_{\tilde{g}}^2 - (m_{\tilde{t}_1} + m_t)^2)} \right) \right]^{1/2}. \quad (16)$$

With $m_{\tilde{g}} = 413$ GeV, $m_{\tilde{\chi}_1^\pm} = 113$ GeV and a top mass of 175 GeV, Eq. (16) gives

$$M^{\max}(tb) \sim 300 \text{ GeV}. \quad (17)$$

The other significant decays at this benchmark point which lead to the same final state are:

$$\tilde{g} \rightarrow \tilde{b}_1 b \rightarrow \tilde{\chi}_1^\pm tb, \quad (18)$$

$$\tilde{g} \rightarrow \tilde{b}_1 b \rightarrow \tilde{t}_1 W b \rightarrow \tilde{\chi}_1^\pm bbW, \quad (19)$$

$$\tilde{g} \rightarrow \tilde{b}_2 b \rightarrow \tilde{\chi}_1^\pm tb, \quad (20)$$

$$\tilde{g} \rightarrow \tilde{b}_2 b \rightarrow \tilde{t}_1 W b \rightarrow \tilde{\chi}_1^\pm bbW. \quad (21)$$

The final states from the decays Eq. (19) and Eq. (21) are equivalent to the final state from the decay Eq. (3) if the bW invariant mass is close to the top mass. Associated gluino production with left or right squark followed by these decays occurs in 4% (Eq. (18)), 9% (Eq. (19)), 0.1% (Eq. (20)) and 0.9% (Eq. (21)) of all SU4 events. Due to the small mass difference between \tilde{g} and the \tilde{b}_1 or \tilde{b}_2 , the final states Eq. (18) and Eq. (19) can be suppressed by imposing a minimum cut on the p_T of the b jet, while the final states Eq. (20) and Eq. (21) are suppressed because b jets originating from the gluino decay $\tilde{g} \rightarrow \tilde{b}_2 b$ are on the average below the detection threshold.

In order to extract light stop signal from the $\tilde{g}\tilde{q}$ events where gluino decays to stop and top, the final state tb invariant mass distribution in Eq. (3) is reconstructed for top quark decays into hadronic final states only:

$$t \rightarrow Wb \rightarrow qqb \quad (22)$$

making no assumptions about the $\tilde{\chi}_1^\pm$ decay modes which dominantly produce two additional light-quark jets. The hardest jet in the event is assumed to be the light-quark jet originating from the decay of the left or right squark produced in association with the gluino.

We select jets with $p_T > 20$ GeV and $|\eta| < 2.5$. In this range the b -tagging efficiency is about 60% [1]. The event selection requires the following:

- At least 5 jets in the event with $p_T > 30$ GeV, where
 - The hardest jet is a light-quark jet with $p_T > 100$ GeV,
 - 2 and only 2 jets are tagged as b jets and they have $p_T > 50$ GeV and
 - At least 2 of the light-quark jets have $p_T > 30$ GeV
- $E_T^{\text{miss}} > 150$ GeV, $M_{\text{eff}} > 400$ GeV, $E_T^{\text{miss}}/M_{\text{eff}} > 0.2$
- $S_T > 0.1$.

Of the Standard Model backgrounds simulated, only events from our $t\bar{t}$ and QCD samples satisfy these selection criteria. No W + jets or Z + jets events pass the cuts.

The dominant detector-performance systematic uncertainties come from the jet and E_T^{miss} energy scale and resolution. Assuming that the uncertainties for 200 pb⁻¹ are the same as for 100 pb⁻¹, i.e. 10% uncertainties on the jet and E_T^{miss} energy scale and resolution [20], and including 5% uncertainty on the b -tagging efficiency, the resulting systematic uncertainty in the number of selected events would be $\sim 40\%$ for SU4 and $\sim 50\%$ for $t\bar{t}$.

The top-bottom invariant mass is reconstructed for events satisfying the selection criteria for the light stop search:

- Excluding the hardest jet, all light-quark jets with $p_T^{\text{jet}} > 30$ GeV are combined into dijet pairs.

Table 6: The number of signal and remaining Standard Model background events and the total event yield at 200 pb^{-1} . The last row gives the signal-to-background ratio. The errors quoted are from detector sources of systematic uncertainty.

$L = 200 \text{ pb}^{-1}$	Initial selection	$ m_{bjj} - m_t < 30 \text{ GeV}$		$\Delta R(t, b) < 2$	
		without W sub.	with W sub.	without W sub.	with W sub.
SU4	963	537	224	267	120
$t\bar{t}$	99	28	13	9	4
QCD	6	3	2	3	2
Total	1068 ± 426	568 ± 225	239 ± 95	279 ± 109	126 ± 50
SU4 / ($t\bar{t}$ + QCD)	9.2 ± 4.1	17.3 ± 7.3	14.9 ± 6.3	22.3 ± 9.1	20.0 ± 8.3

- All such pairs with invariant mass within the window $|m_{jj} - m_W| < 15 \text{ GeV}$ are combined with each of the two b jets and the bjj combination with invariant mass closest to the top mass is selected.
- The four-vectors of this dijet pair are rescaled such that $m_{jj} = m_W$ and m_{bjj} is recalculated and accepted as top candidate if $|m_{bjj} - m_{top}| < 30 \text{ GeV}$.
- The same bjj combination is combined with the other b jet and m_{tb} calculated, with the requirement that the angle between top and bottom be $\Delta R(t, b) < 2$.

The W sideband method [21–23] is used to estimate SUSY combinatorial background originating from supersymmetric processes in which jet pairs accidentally have an invariant mass within our W -mass window, and so fake W bosons. The sidebands used are the regions of dijet invariant mass 30 GeV below and 30 GeV above our W -mass window. The fake W boson contribution to the m_{tb} distribution is evaluated as the average contribution of the jet pairs from the W sidebands after they have been scaled linearly to the W mass zone and the procedure of m_{tb} reconstruction has been repeated.

The numbers of signal and the remaining Standard Model background events, together with the total event yield at 200 pb^{-1} , are listed in Table 6. The m_{tb} distribution reconstructed in signal events without the subtraction of the SUSY combinatorial background and the SUSY combinatorial background itself are plotted in Figure 10. The contribution of fake W bosons in SU4 is higher than the number of events remaining after subtraction.

The m_{tb} distributions before and after the subtraction of the SUSY combinatorial background are shown in Figure 10. The background-subtracted distribution is fitted in order to extract the endpoint. The resulting m_{tb} distribution is fitted with a triangular function smeared with a Gaussian:

$$f(M) = A \int_{-1}^1 e^{-\frac{(M - M^{\max} \sqrt{\frac{1+x}{2}})^2}{2\sigma^2}} dx + (a + bM),$$

where the kinematic endpoint, M^{\max} , and the smearing, σ , are two of the five fit parameters. The smearing, σ , models the experimental resolution of the reconstructed m_{tb} . The position of the upper kinematic endpoint obtained from the 5-parameter fit (Figure 10) is $M^{\max} = 297 \pm 9 \text{ GeV}$ with $\sigma = 28 \pm 7 \text{ GeV}$ corresponding to $\sim 10\%$ of the M^{\max} value. The position of the upper kinematic endpoint obtained from the 4 parameters fit is $M^{\max} = 298 \pm 6(\text{stat})_{-41}^{+16}(\text{sys}) \text{ GeV}$ with σ set to 10% of M^{\max} . The expected value of m_{tb} given by Eq. (17) is 300 GeV .

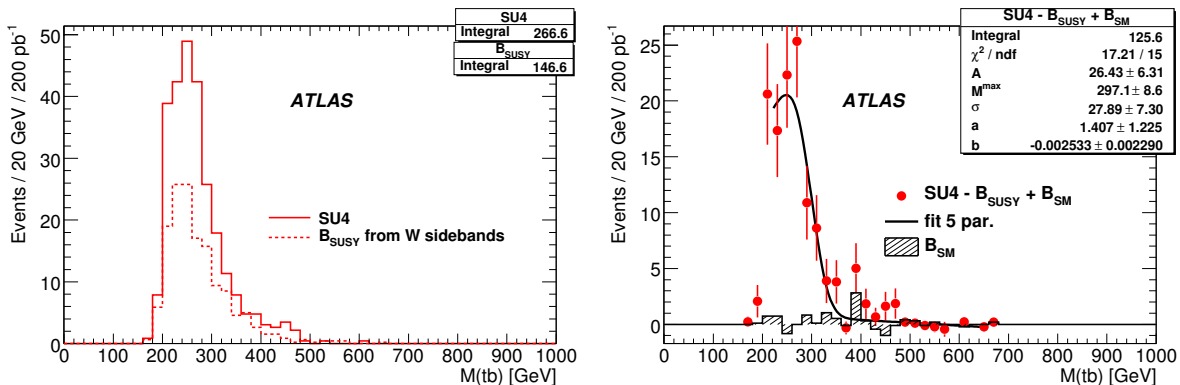


Figure 10: Left: Reconstructed m_{tb} distributions in signal and SUSY combinatorial background events. Right: The 5 parameters fit of the sum of the reconstructed m_{tb} distributions in signal and the remaining Standard Model events after the subtraction of the SUSY combinatorial background; all at 200 pb^{-1} .

8 Higgs signatures in SUSY events

In the context of supersymmetric models, Higgs bosons at the LHC can be produced in proton collisions either through direct interaction of Standard Model particles, such as gluon-gluon fusion, or through the decay of a supersymmetric particle produced in the initial interaction.

We will consider the possibility of observing the lightest CP-even h boson via the second mechanism. In this case, a missing transverse energy signature, typical of R-parity conserving SUSY scenarios, can be reconstructed in association with the Higgs boson and exploited to reduce the background, making it possible to study the dominant decay channel $h \rightarrow b\bar{b}$, which is otherwise hidden by the enormous QCD continuum.

Within mSUGRA the most promising source of Higgs production is the decay of a second-lightest neutralino. Indeed, $\tilde{\chi}_2^0 \rightarrow \tilde{\chi}_1^0 h$, if open, dominates the $\tilde{\chi}_2^0 \rightarrow \tilde{\chi}_1^0 Z$ mode, because the two lightest neutralinos are basically gauginos, so that the higgsino-gaugino-Higgs vertex is enhanced with respect to the higgsino-higgsino-gauge one. However, if the sleptons are lighter than the $\tilde{\chi}_2^0$, the decay channels $\tilde{\ell}^\pm \ell^\mp$ and $\tilde{\nu}_\ell \bar{\nu}_\ell$ open up, dominating the $\tilde{\chi}_2^0$ width. As a consequence, we expect that mSUGRA points interesting for Higgs searches will not show a clear di-lepton signature. The benchmark point chosen for this analysis is SU9, at which $BR(\tilde{\chi}_2^0 \rightarrow \tilde{\chi}_1^0 h) \sim 87\%$.

Exploiting the capabilities of the ATLAS detector in missing transverse energy measurement and b tagging, the passage of weakly interacting particles may be revealed and a $b\bar{b}$ pair with invariant mass peaking around the Higgs mass can be reconstructed.

Standard Model events with similar signatures which are backgrounds for this analysis, include events with neutrino production causing a genuine E_T^{miss} signal and QCD events with fake E_T^{miss} generated by instrumental effects. SUSY events can themselves constitute a background, as they contain many b -jet candidates, both true and mistagged. These can be divided into two categories: SUSY cascades without and with production of a Higgs decaying to $b\bar{b}$. In the latter case potential signal events may be incorrectly reconstructed as the selected $b\bar{b}$ pair is not the one coming from the Higgs decay. We will refer to the former type simply as ‘‘SUSY background’’ and to the latter as ‘‘combinatorial background’’.

The following selection cuts are applied:

1. $E_T^{\text{miss}} > 300 \text{ GeV}$;

2. two light-flavoured jets with $p_T > 100$ GeV;
3. two b jets with $p_T > 50$ GeV;
4. no leptons with $p_T > 10$ GeV.

The first two cuts are typical of SUSY analyses, while the purpose of the last cut is to suppress backgrounds from $t\bar{t}$ and W production.

When three or more b jets with transverse momentum greater than 50 GeV are found in a single event, the second and third leading- p_T b -jets are chosen as the candidate Higgs decay pair. This is because an important source of b jets is the decay of a bottom squark to $\tilde{\chi}_2^0$ and b and since $m_{\tilde{b}} - m_{\tilde{\chi}_2^0} \sim 500$ GeV $> m_h$ the sbottom daughters get more allowed phase space than the Higgs daughters and thus, in general, higher p_T .

In Figure 11 (left) the invariant mass of the selected b jet pairs is shown assuming 10 fb^{-1} of collected luminosity. The shaded histogram corresponds to the sum of the Standard Model backgrounds, the dashed and dotted lines are the SUSY and combinatorial backgrounds respectively. These last two, together with the $t\bar{t}$ production, are the most important backgrounds. The black curve is the result of a least squares fit to a Gaussian function, representing the Higgs resonance, superimposed on a second degree polynomial background. The estimated number of signal and background events is obtained by counting the b pairs with invariant mass inside a ± 25 GeV range around the fitted peak centre. The signal significance, computed in the Gaussian approximation as the number of signal events over the square root of the background, is about 14.

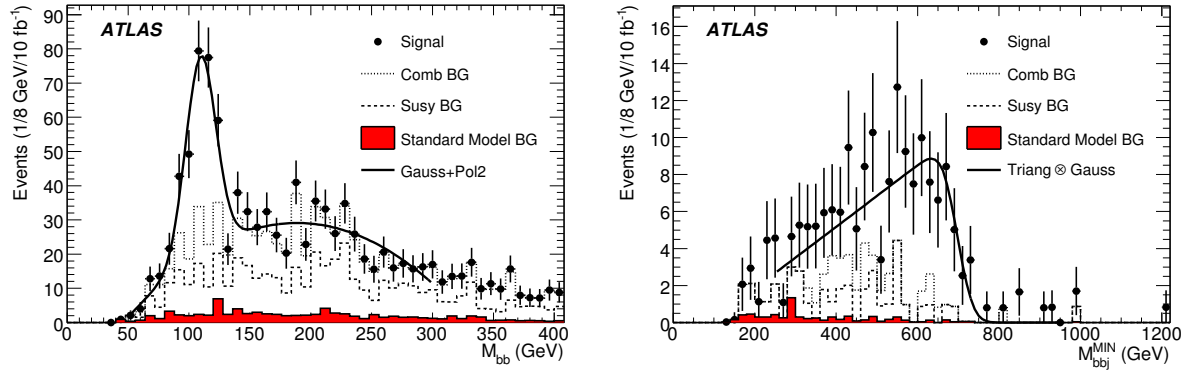


Figure 11: Invariant mass of the selected b -jet pairs (left) and invariant mass of the system consisting of the Higgs plus the jet minimising m_{hq} (right) for 10 fb^{-1} of integrated luminosity.

Table 7 summarises the expected event rates after the application of the selection cuts and after the additional mass window request.

SUSY mass spectrum information is reconstructed in the SU9 model by studying the decay:

$$\tilde{q}_L \rightarrow \tilde{\chi}_2^0 q \rightarrow \tilde{\chi}_1^0 h q. \quad (23)$$

As a consequence of two-body kinematics, the invariant mass of the Higgs-quark system shows both a minimum and a maximum value, related to different combinations of the masses of the SUSY particles involved.

The events passing the previous selection cuts, including the mass window cut, are also required to have at least one b jet with $p_T > 100$ GeV. Furthermore, a veto is imposed on additional b -tagged jets

Table 7: Summary of the number of expected SUSY and Standard Model events after the application of the different selection cuts, for 10 fb^{-1} of integrated luminosity.

SU9	Signal	Comb BG	Susy BG	
No cuts		11050	21950	
Cut 1, 2, 3	356	946	908	
Cut 4	230	449	433	
$\pm 25 \text{ GeV}$ mass window	179	76	76	
Standard Model	$t\bar{t}$	Z	W	bb
Cut 1, 2, 3	133	12	22	43
Cut 4	53	8	10	21
$\pm 25 \text{ GeV}$ mass window	11	2	4	4

with $p_T > 50 \text{ GeV}$. This will result in fewer signal events, but also in a reduced background contamination yielding a clear distribution shape, albeit with lower signal significance. As in Section 4 the quark from the \tilde{q}_L is expected to produce one of the two highest- p_T jets and the two distributions m_{hq}^{\min} and m_{hq}^{\max} are reconstructed using the jet that maximises and minimises the m_{hq} value, respectively. Since the background events will tend to concentrate toward low mass values, the m_{hq}^{\min} (Figure 11, right) is used to determine the mass upper limit $m_{hq,\text{edge}}$. The $m_{hq,\text{threshold}}$ value can be determined from the m_{hq}^{\min} distribution.

The mass edge value is obtained by fitting a triangular shape convolved with a Gaussian:

$$m_{hq,\text{edge}} = 695 \pm 15 \text{ (stat)} \pm 3 \text{ (syst)} \pm 35 \text{ (JES)},$$

to be compared to the true value of 732 GeV . The statistical uncertainty is the error on the fitted parameter, while the systematic comes from the parameter dependence on the fitting boundaries. An additional 5% systematic error is expected from the jet energy scale (JES) uncertainty.

The mass threshold evaluation is more challenging, since background events tend to populate the low mass region. For an integrated luminosity of 10 fb^{-1} , it was not possible to fit to the mass distribution. However, high-statistics studies performed with a fast simulation of the ATLAS detector show that a mass threshold value could be extracted from 300 fb^{-1} of collected data, expected after 3 years of LHC running at design luminosity.

9 Mass and parameters measurement

This section is devoted to the extraction of SUSY mass spectra and parameters from the measurements described in the previous sections of this note. As an example, the mSUGRA benchmark points SU3 (with a luminosity of 1 fb^{-1}) and SU4 (with 0.5 fb^{-1}) are chosen to give a flavour of what might be expected in the initial phase of the experiment in case of a rather optimistic SUSY scenario. The small luminosity at this stage results in a limited number of available measurements and rather large uncertainties. In such a situation only models with few parameters can be fitted. In Section 9.1 the masses of the decay chain Eq. (1) are derived from the measurement of the kinematic endpoints described in Section 3 and 4. In Sections 9.2 to 9.4 the parameters of the mSUGRA model are derived instead.

9.1 Measurement of masses from SUSY decays

We use the information from the experimentally measured endpoints to extract the masses of the SUSY particles. As described earlier in this paper, in many cases analytic expressions have been deduced for the endpoints expressed in terms of the masses. Examples are shown in Eq. (4) and Eq. (5). If sufficient endpoints are known, then the masses can be deduced. Here we use a numerical χ^2 minimization based on the MINUIT package to extract the SUSY particle masses from a combination of endpoints. We define the χ^2 as

$$\chi^2 = \sum_{k=1}^n \frac{(m_k^{\max} - t_k^{\max}(m_{\tilde{\chi}_1^0}, m_{\tilde{\chi}_2^0}, m_{\tilde{\ell}_R}, m_{\tilde{q}_L}))^2}{\sigma_k^2}. \quad (24)$$

For each of the n endpoint measurements, k , the quantities m_k^{\max} and σ_k denote the fit value and its uncertainty respectively. The t_k^{\max} are the theoretical endpoint expressions [6, 10], which contain as parameters the masses of the two lightest neutralinos, the scalar quark \tilde{q}_L , and (for the two-body decay chain only) the scalar lepton $\tilde{\ell}_R$. As a starting point for the fit the generated masses are used. The masses are constrained to be positive in the fit and the mass hierarchies from the model input are enforced.

With the statistics expected for an integrated luminosity of 1 fb^{-1} (0.5 fb^{-1}) for SU3 (SU4) we observe instabilities in the fit. Depending on the fluctuation and precision of the endpoint measurements the fit does not converge. Some of the measured endpoints have shown possible deviations from the generated values of up to several standard deviations. Systematic effects to explain such discrepancies are identified in earlier sections of this article. Significant deviations distort the results and also negatively affect the fit convergence, especially in the presence of degenerate kinematic endpoint equations. We also note large correlations (typically larger than 95%) among the fitted parameters. This is expected, since the endpoints are most sensitive to mass differences. The correlations can also lead to difficulties with convergence and result in larger uncertainties for the fitted masses.

To show a potential result with early data, we quote here the results from converging fits for both the SU3 and SU4 points. We use the endpoints from the lepton+jets edges summarized in Table 4 and the dilepton edge fit from Section 3 ($99.7 \pm 1.4 \pm 0.3 \text{ GeV}$ for SU3 and $52.7 \pm 2.4 \pm 0.3 \text{ GeV}$ for SU4). For the SU3 fit, all dilepton+jets edges are used. In the SU4-fit, we discard the $m_{\ell q(\text{low})}$ measurement as it has been shown not to be very reliable and does not provide additional constraints in three-body decay scenarios such as SU4. The $m_{\ell q(\text{high})}$ endpoint can be measured more reliably and its kinematic expression only differs from the one of $m_{\ell q(\text{low})}$ by a constant factor. The di-tau edges are not used here.

The masses resulting from the χ^2 fit are shown in Table 8 (upper part). The parabolic errors are the first errors shown in the table and the jet energy scale errors are the second. Asymmetric errors show a large uncertainty on the positive side. The jet energy scale errors are determined by varying all the endpoints along with their fully correlated jet energy scale uncertainties and refitting the masses. The difference in the central values of the fit is taken as the jet energy scale uncertainty for Table 8. One can see that the jet energy scale errors are small compared to the error on the masses, but might be relevant to the mass difference measurements.

We note that a fit with SU3 kinematic assumptions applied to the SU4 endpoints also returns consistent masses. The decision about the mass hierarchy would thus have to be based on additional information from collider data. A possible source is the shape of the dilepton edge as discussed in Section 3.

Besides the masses we can also extract differences of SUSY particle masses. These are more directly related to the endpoints and we expect to be able to determine them more reliably than the masses of individual sparticles. For mass differences, a χ^2 similar to Eq. (24) is used, where the parameters are written in terms of mass differences to the neutralino $\tilde{\chi}_1^0$. We obtain the results shown in Table 8 (bottom part).

We conclude that a first look at sparticle masses is possible with early data, although with large uncertainties. Appropriate model assumptions and additional information will probably have to be used

Table 8: Resulting SUSY particle masses and mass differences within SU3 and SU4 from the χ^2 minimization fit using the dilepton and lepton+jets edges. Shown are the measured masses m_{meas} and mass differences Δm_{meas} followed first by the parabolic errors as returned by MIGRAD and then by the jet energy scale errors. When the measured parameter is anticorrelated with the jet energy scale variation, this is indicated by a \mp sign. The input Monte Carlo masses m_{MC} and mass differences Δm_{MC} are also shown. The integrated luminosity assumed is 1 fb^{-1} for SU3 and 0.5 fb^{-1} for SU4.

Observable	SU3 m_{meas} [GeV]	SU3 m_{MC} [GeV]	SU4 m_{meas} [GeV]	SU4 m_{MC} [GeV]
$m_{\tilde{\chi}_1^0}$	$88 \pm 60 \mp 2$	118	$62 \pm 126 \mp 0.4$	60
$m_{\tilde{\chi}_2^0}$	$189 \pm 60 \mp 2$	219	$115 \pm 126 \mp 0.4$	114
$m_{\tilde{q}}$	$614 \pm 91 \pm 11$	634	$406 \pm 180 \pm 9$	416
$m_{\tilde{\ell}}$	$122 \pm 61 \mp 2$	155		
Observable	SU3 Δm_{meas} [GeV]	SU3 Δm_{MC} [GeV]	SU4 Δm_{meas} [GeV]	SU4 Δm_{MC} [GeV]
$m_{\tilde{\chi}_2^0} - m_{\tilde{\chi}_1^0}$	$100.6 \pm 1.9 \mp 0.0$	100.7	$52.7 \pm 2.4 \mp 0.0$	53.6
$m_{\tilde{q}} - m_{\tilde{\chi}_1^0}$	$526 \pm 34 \pm 13$	516.0	$344 \pm 53 \pm 9$	356
$m_{\tilde{\ell}} - m_{\tilde{\chi}_1^0}$	$34.2 \pm 3.8 \mp 0.1$	37.6		

to constrain the fits.

9.2 Observables and fit assumptions

To demonstrate the feasibility of parameter determination with initial data, we show the constraints one would obtain for our benchmark points if one assumed an mSUGRA framework.

The SUSY parameter-fitting package Fittino version 1.4.1 [24] is used, interfaced to a beta version of SPheno3 [25] to perform the theoretical calculations for a given set of parameters.

The fit is given the measurements presented in sections 3, 4 and 6. The lepton and the jet energy scale uncertainties are each considered to be 100% correlated between measurements. Uncertainties on the theoretical predictions are not taken into account. For illustration purposes an additional parameter determination is performed where – following a prescription used in [26] – 1% (0.5%) uncertainty on the theoretical calculation of the pole masses of coloured (un-coloured) sparticles is assumed. No correlations between the theoretical uncertainties on the pole masses are considered.

9.3 Markov chain analysis

To obtain a first glimpse of the possible parameter space a Markov chain analysis is performed. With this technique it is possible to efficiently sample from a large-dimensional parameter spaces. This allows us to check whether there are several topologically disconnected parameter regions which are favoured by the given measurements.

Figure 12 shows two-dimensional likelihood maps for M_0 and $M_{1/2}$ (left) as well as $\tan\beta$ and A_0 (right) for sign $\mu = +1$ obtained for the given set of measurements. The plots demonstrate that for a given sign μ preferred parameters are found around the true parameter points independent of the starting point. No further preferred regions occur. For M_0 and $M_{1/2}$ a clearly preferred region is found around the SU3 values of 100 GeV and 300 GeV, respectively. As expected, given the measurements used, the determination of $\tan\beta$ and A_0 is more difficult. Nevertheless, here too the region around the nominal

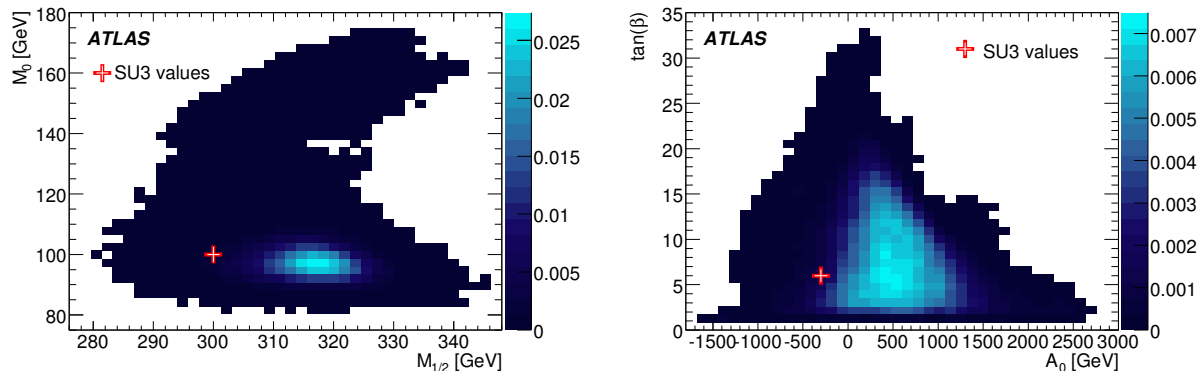


Figure 12: Two-dimensional Markov chain likelihood maps for mSUGRA parameters M_0 and $M_{1/2}$ (left) as well as $\tan\beta$ and A_0 (right) for sign $\mu = +1$, for benchmark point SU3, with integrated luminosity of 1 fb^{-1} . The crosses indicate the actual values of the parameters for that benchmark point.

SU3 values is the preferred one.

9.4 Parameter determination

In order to determine the derived central values of the parameters and their uncertainties, for each assumption of the sign of μ a set of 500 toy fits are performed. For each fit the observables are smeared using the full correlation matrix. Simulated annealing followed by a Minuit fit started with the best parameter estimates from simulated annealing is subsequently run using the smeared observables. The four-dimensional distribution of parameters obtained from the toy fits is used to derive the parameter uncertainties and their correlations. Figure 13 shows the one-dimensional projections of parameter distributions for M_0 , $M_{1/2}$, $\tan\beta$ and A_0 . The mean and RMS values of the results of the fit are reported in Table 9. As already indicated by the Markov chain analysis M_0 and $M_{1/2}$ can be derived reliably with uncertainties $\pm 9.3 \text{ GeV}$ and $\pm 6.9 \text{ GeV}$ (RMS of the toy fit results), respectively whereas for $\tan\beta$ and A_0 only the order of magnitude can be derived from these measurements. The χ^2 distribution of the toy fits can be used to evaluate the toy fit performance. The observed mean $\chi^2 = 12.6 \pm 0.2$ for sign $\mu = +1$ is compatible with the expected value of $N_{dof} = 11$. The solutions for the wrong assumption sign $\mu = -1$, also reported in Table 9, cannot however be ruled out as the observed mean $\chi^2 = 15.4 \pm 0.3$ is also acceptable.

10 Conclusions

If the supersymmetric partners of quarks and gluons exist at a moderate mass scale ($\lesssim 1 \text{ TeV}$) they will be abundantly produced in pp collisions at the LHC centre-of-mass energy of 14 TeV . In this scenario, a few fb^{-1} of ATLAS data will allow the discovery of the new particles [1], once the commissioning of the detector has been completed and the Standard Model backgrounds have been well understood.

The next step after discovery will be to select specific supersymmetric decay chains to measure the properties of the new particles. Here we have focused on those measurements that will be possible using 1 fb^{-1} of integrated luminosity. Specific benchmarks in parameter space have been used to demonstrate the precision that can be expected from these measurements, but the same (or similar) techniques can be applied to much of the SUSY parameter space accessible with early LHC data.

Table 9: Results of a fit of the mSUGRA parameters to the observables listed in Sections 3, 4 and 6 for the SU3 point. The mean and RMS of the distribution of the results from the toy fits is reported. The two possible assumptions for the digital parameter $\text{sign}(\mu) = +1$ $\text{sign}(\mu) = \pm 1$ have been used, resulting in different preferred regions for the other parameters. The effect of different assumptions on theoretical uncertainties is also shown.

Parameter	SU3 value	fitted value	exp. unc.
$\text{sign}(\mu) = +1$			
$\tan\beta$	6	7.4	4.6
M_0	100 GeV	98.5 GeV	± 9.3 GeV
$M_{1/2}$	300 GeV	317.7 GeV	± 6.9 GeV
A_0	-300 GeV	445 GeV	± 408 GeV
$\text{sign}(\mu) = -1$			
$\tan\beta$		13.9	± 2.8
M_0		104 GeV	± 18 GeV
$M_{1/2}$		309.6 GeV	± 5.9 GeV
A_0		489 GeV	± 189 GeV

For the benchmark points considered, the most promising decay chain involves the leptonic decay of the next-to-lightest neutralino ($\tilde{\chi}_2^0 \rightarrow \tilde{\chi}_1^0 \ell^+ \ell^-$). The invariant mass of the two leptons shows a clear kinematic maximum (Section 3) which could already be measured with a precision of a few per cent with the limited data set considered. The combination of one or both leptons with the hardest jets in the event would allow observation of several other kinematic minima and maxima (Section 4).

For high values of $\tan\beta$ the decays into taus will be far more abundant than those involving electrons or muons; the excellent performance expected for the identification and measurement of hadronic τ decays in ATLAS will also allow observation of the dilepton edge in the $\tau^+ \tau^-$ invariant mass distribution (Section 5).

The leptonic decays will not be the only channel for early measurements with supersymmetric decays. The $\tilde{q}_R \rightarrow q \tilde{\chi}_1^0$ decay can be used to determine the \tilde{q}_R mass (Section 6). The combination of hadronically decaying top quarks and b -jets in supersymmetric events is also a promising possibility for low-scale Supersymmetry with decay chains involving scalar top and bottom quarks, as shown by the reconstruction of the edge of the $t\bar{b}$ invariant mass discussed in Section 7.

If the $\tilde{\chi}_2^0 \rightarrow \tilde{\chi}_1^0 h$ decay is open, it will provide a substantial source of Higgs bosons. Since the Standard Model backgrounds can be suppressed by the usual SUSY cuts, it will then become possible to observe the $h \rightarrow b\bar{b}$ decay with moderate (5 fb^{-1}) integrated luminosity (Section 8).

The different channels will provide complementary information about the SUSY mass phenomenology. The various measurements will have to be combined to reconstruct the SUSY mass spectrum and attempt to understand the SUSY-breaking mechanism. In Section 9 it is discussed how a selected set of early studies can be combined to obtain the first measurements of supersymmetric masses and of the parameters of the mSUGRA model. With 1 fb^{-1} the reconstruction of part of the supersymmetric mass spectrum will only be possible for favourable SUSY scenarios and with some assumptions about the decay chains involved. Larger integrated luminosity will help to overcome these limitations, as more measurements become possible and the precision of each increases.

References

- [1] ATLAS Collaboration, *Prospects for SUSY discovery based on inclusive searches*, this volume.
- [2] ATLAS Collaboration, *Supersymmetry searches with ATLAS*, this volume.
- [3] ATLAS Collaboration, *Supersymmetry signatures with high p_T photons or long-lived heavy particles*, this volume.
- [4] M. N. Nojiri, Y. Yamada, Phys. Rev. D **60** (1999) 015006.
- [5] U. De Sanctis, T. Lari, S. Montesano, C. Troncon, Eur. Phys. J. C **52** (2007) 743.
- [6] B. C. Allanach, C. G. Lester, M. A. Parker and B. R. Webber, JHEP **0009** (2000) 004.
- [7] C. G. Lester, M. A. Parker and M. J. White, JHEP **0710** (2007) 0051.
- [8] ATLAS Collaboration, *Reconstruction and identification of electrons in ATLAS*, this volume.
- [9] ATLAS Collaboration, *Muon reconstruction and identification performance in ATLAS: studies with simulated Monte Carlo samples*, this volume.
- [10] B. K. Gjelsten, D. J. Miller, P. Osland, JHEP **0412** (2004) 003.
- [11] D. J. Miller and P. Osland and A. R. Raklev, JHEP **0603** (2006) 034.
- [12] C.G. Lester, Phys. Lett. **B655** (2007) 39–44.
- [13] ATLAS Collaboration, *Reconstruction and identification of hadronic tau decays with ATLAS*, this volume.
- [14] D. J. Mangeol, U. Goerlach, Search for $\tilde{\chi}_2^0$ decays to $\tilde{\tau}\tau$ and SUSY mass spectrum measurement using di- τ final states, 2006, CMS NOTE 2006/096.
- [15] Richter-Was, Elzbieta and Froidevaux, Daniel and Poggioli, Luc, *ATLFAST 2.0 a fast simulation package for ATLAS* Atlas Note ATL-PHYS-98-131.
- [16] S. Y. Choi, K. Hagiwara, Y. G. Kim, K. Mawatari and P. M. Zerwas, Phys. Lett. B **648** (2007).
- [17] A.J. Barr, C.G. Lester, P. Stephens, J.Phys.G **29** (2003) 2343.
- [18] C.G. Lester, D. Summers, Phys.Lett.B **463** (1999) 99.
- [19] J. Krstic, M. Milosavljevic and D. Popovic, *Studies of a low mass SUSY model at ATLAS with full simulation*, ATL-PHYS-PUB-2006-028.
- [20] ATLAS Collaboration, *Data-driven determinations of W, Z, and top background to supersymmetry*, this volume.
- [21] J. Hisano, K. Kawagoe and M.M. Nojiri, Phys. Rev. D **68** (2003) 035007.
- [22] J. Hisano, K. Kawagoe and M.M. Nojiri, *A Detailed Study of the Gluino Decay into the Third Generation Squarks at the CERN LHC*, ATL-PHYS-2003-29.
- [23] ATLAS Collaboration, *ATLAS detector and physics performance. Technical design report Vol. 2*, CERN-LHCC-99-15 (1999).

- [24] P. Bechtle, K. Desch, and P. Wienemann, *Comput. Phys. Commun.* **174** (2006) 47–70.
- [25] W. Porod, *Comput. Phys. Commun.* **153** (2003) 275–315.
- [26] R. Lafaye, T. Plehn, M. Rauch and D. Zerwas, *Eur. Phys. J.* **C54** (2008) 617–644.

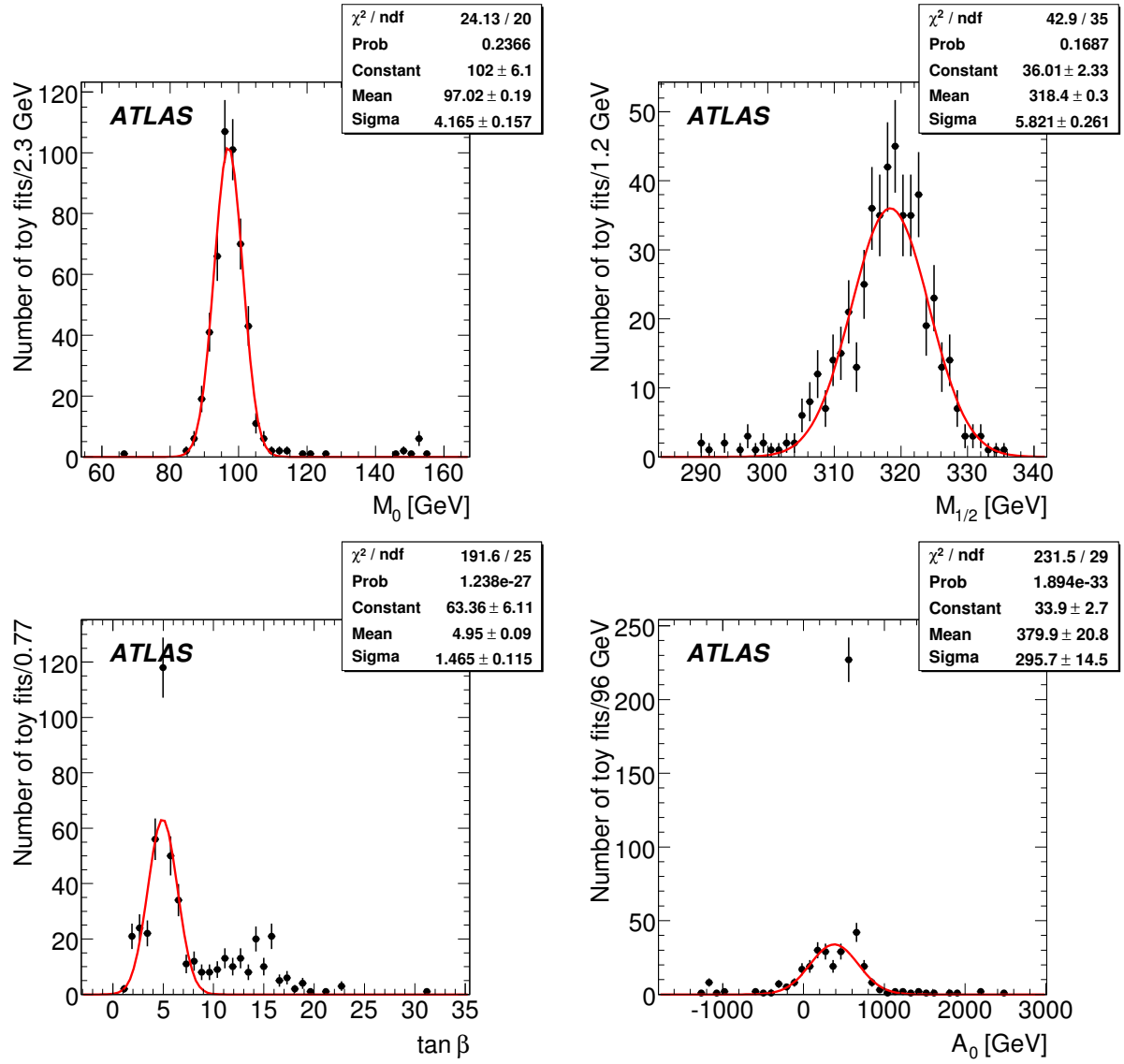


Figure 13: Distributions of the mSUGRA parameters obtained with the fits to pseudo-experiment results.